A weak compatibility condition for precipitation with application to the microstructure of PbTe–Sb$_2$Te$_3$ thermoelectrics

Xian Chen [a], Shanshan Cao [b,1], Teruyuki Ikeda [c], Vijay Srivastava [a], G. Jeffrey Snyder [d],
Dominique Schryvers [b], Richard D. James [a,*]

[a] *Department of Aerospace Engineering and Mechanics, 107 Akerman Hall, University of Minnesota, Minneapolis, MN 55455, USA*
[b] *Electron Microscopy for Materials Science (EMAT), University of Antwerp, Antwerp, Belgium*
[c] *PRESTO, Japan Science and Technology Agency, 4-1-8 Honcho, Kawaguchi, Saitama 332-0012, Japan*
[d] *Materials Science, California Institute of Technology, 1200 E. California Blvd., Pasadena, CA 91125, USA*

Abstract

We propose a weak condition of compatibility between phases applicable to cases exhibiting full or partial coherence and Widmanstätten microstructure. The condition is applied to the study of Sb$_2$Te$_3$ precipitates in a PbTe matrix in a thermoelectric alloy. The weak condition of compatibility predicts elongated precipitates lying on a cone determined by a transformation stretch tensor. Comparison of this cone with the long directions of precipitates determined by a slice-and-view method of scanning electron microscopy combined with focused ion beam sectioning shows good agreement between theory and experiment. A further study of the morphology of precipitates by the Eshelby method suggests that interfacial energy also plays a role and gives an approximate value of interfacial energy per unit area of 250 dyn cm^{-1}.
© 2011 Acta Materialia Inc. Published by Elsevier Ltd. All rights reserved.

Keywords: Compatibility; Precipitation; Widmanstätten microstructure; Thermoelectric materials

1. Introduction

In martensitic phase transformations it has been appreciated since the 1950s that elastic compatibility plays an important role in determining the morphology of microstructure resulting from the phase transformation [1–4]. Recently, new links have been established between conditions of compatibility and other properties of transforming materials, such as thermal hysteresis [5,6], thermal stability and fatigue under repeated transformation [7], magnetocaloric properties [8] and energy conversion efficiency [9,10]. For example, in TiNiCuPd alloys whose composition has been tuned to satisfy the special compatibility condition $\lambda_2 = 1$, where λ_2 is the middle eigenvalue of the transformation stretch matrix [2,5], it is found that the thermal hysteresis drops precipitously from about 60 K to near zero as $\lambda_2 \to 1$. From a physical viewpoint the condition $\lambda_2 = 1$ implies that the austenite fits perfectly onto the martensite, or, more precisely, a part of the austenite can transform to unstressed martensite while remaining perfectly matched with the martensite at an interface. Mathematically, λ_2 is the middle eigenvalue of the positive-definite symmetric matrix $\mathbf{C} = \mathbf{F}^T\mathbf{F}$, where ^{T} denotes the transpose and $\mathbf{F}$ is a linear transformation that maps a suitable unit cell of the austenite lattice to the corresponding unit cell of the martensite lattice (see [5] for further details). In TiNiPd the existence of the corresponding compatible interface between austenite and a single variant of martensite was confirmed [11] by high-resolution transmission electron microscopy. Other examples of a significant relation

---

* Corresponding author. Tel.: +1 6126250706.
  E-mail address: james@umn.edu (R.D. James).
[1] Present address: Department of Metallic Materials, School of Materials Science and Engineering, South China University of Technology, 381 Wushan Road, Guangzhou 510640, People's Republic of China.

between $\lambda_2 \approx 1$ and properties are emerging in Heusler alloys [12,13], oxides [14], multiferroic materials [15], battery materials [16] and oxyacid materials used in fuel cells [17].

Diffusional phase transformations, particularly those which show clear evidence of dislocations at the boundary of precipitates and therefore are considered semicoherent at best, are not thought to be influenced by conditions of elastic compatibility. We explore in this paper a weaker condition of compatibility between phases than $\lambda_2 = 1$ in the context of a diffusional phase transformation in the thermoelectric system PbSbTe. In this system Sb_2Te_3 Widmanstä tten type precipitates grow in a PbTe matrix [18]. A typical lattice mismatch is 6.2%. Thermoelectric composites with microstructures having small length scales are expected to exhibit reduced lattice thermal conductivity due to the scattering of long mean-free-path phonons at interfaces [19]. Low lattice thermal conductivity has been observed [20] in composites containing nanoparticles (≈ 5 nm) but also in samples with micron sized (≈ 2 µm) particles [21] similar in size to those studied in this work. Control of both carrier type and concentration as well as thermal conductivity is critical in thermoelectric materials. Phonon scattering at interfaces is believed to be important, leading to lowered thermal conductivity while not compromising electrical properties. It has also been demonstrated in superlattices that the density of coherent interfaces plays an important role in reducing thermal conductivity [22].

The condition $\lambda_2 = 1$ is necessary and sufficient for the two unstressed phases to coexist across an interface, after a possible rigid body rotation of one of the phases. In the context of geometrically nonlinear theories of elastic phase transformation [2], $\lambda_2 = 1$ is equivalent to a "rank-one connection" between energy wells: two deformation gradients on different wells differ by a rank-one matrix. The weaker condition of compatibility we study in this paper is equivalent to a "rank-two connection". This condition predicts the elongation of precipitates during coarsening. In the present case the long direction of these precipitates is predicted to lie on one of four crystallographically equivalent cones. The angle of these cones is predicted from the lattice parameters of the two phases.

These ideas can be critically examined owing to recent advances [23,24] on the slice-and-view method of scanning electron microscopy (SEM) combined with focused ion beam (FIB) sectioning. In the present case we used this method to reconstruct the 3-D morphology of the Sb_2Te_3 precipitates in a $(5 \, \mu m)^3$ box. When the end-to-end vectors of 27 of the larger precipitates were plotted in 3-D, we found they were close to the predicted cone, with a standard deviation of 2.94°.

While the largest precipitates were needle-like, the medium-sized precipitates, besides being elongated, were also flattened in a perpendicular direction. Small precipitates were primarily flattened, with little elongation, and the smallest precipitates were approximately spheroidal. This motivated a finer analysis using the Eshelby method in

the geometrically linear context, together with an interfacial energy. This shows qualitative agreement with the secondary aspects of the morphology of the precipitates. It also suggests an approximate value for the interfacial energy constant in this material, 250 dyn cm^{-1}. We carefully describe the transition of geometrically nonlinear to geometrically linear theory in this context, which involves the determination of a certain free angle.

The fact that the rank-two connection predicts well the overall morphology of the two phases suggests that any method that alters the lattice parameters of the two phases so as to modify the undistorted cone will influence the morphology. For example, heat treatment under stress is suggested by the present study and earlier studies on related precipitation reactions [24]. This also affects the Eshelby calculation, and therefore the flattening normal to the axis of elongation. These predictions can therefore provide simple guidelines for heat treatment procedures that place a lot of interfacial area of highly coherent interfaces perpendicular to the eventual direction of heat flow, therefore improving the thermoelectric effect.

In this paper tensors (matrices) are written as uppercase bold letters, and vectors as lowercase, italic, bold letters. The notation $\boldsymbol{a} \otimes \boldsymbol{b}$ denotes the tensor with components $a_i b_j$, written in the basis for which $\boldsymbol{a}$ has components a_k and $\boldsymbol{b}$ has components b_k. $\mathbf{I}$ is the identity matrix.

2. Experimental methods and characterization of the geometry of the precipitates

An alloy with nominal composition $(PbTe)_{0.94}$ $(Sb_2Te_3)_{0.06}$ was prepared by melting Pb, Sb and Te (99.999% purity) for 600 s in fused quartz tubes and homogenizing by annealing at 570 °C for 7 days. To induce precipitation, the sample was annealed at 450 °C for 38 h, followed by water quenching. The details of the sample preparation procedure are described elsewhere [25].

This $PbTe/Sb_2Te_3$ sample was prepared for study using a dual beam focused ion beam/scanning electron microscope (DB FIB/SEM) with serial sectioning as described in detail in Ref. [23]. The bulk sample was placed at the eucentric point of the stage where the Ga^+ ion and electron beams converge. A 5 µm × 5 µm × 5 µm sample box surrounded by a U-shaped open region was defined by etching with Ga^+ ions. During this preliminary excavation, the top surface was protected by a Pt coating. Subsequently, the box was sliced by etching with focused Ga^+ ions, each slice having a thickness of 25 nm, for a total of 200 slices. The slices were viewed sequentially by optimized secondary electron (SE) imaging. The precipitates showed good contrast on the freshly exposed surfaces, making pixelization easy. The 3-D microstructure of the whole box was reconstructed as shown in Fig. 1.

In order to quantify the shapes of the precipitates for further analysis, we fit the shapes of a subset of precipitates to ellipsoids in the following way. For each chosen precipitate we first identified the pixels on the boundary of the
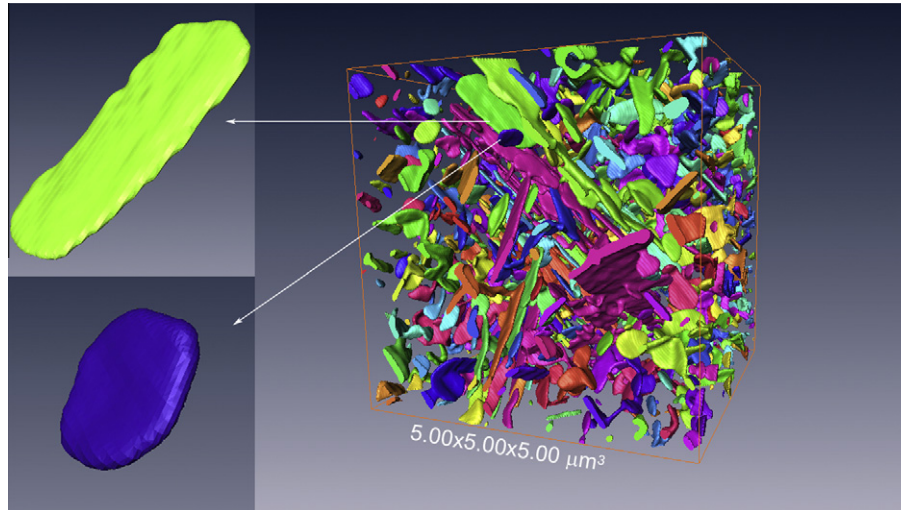
Fig. 1. Reconstruction of precipitates. The inserts show large (inset, top) and small (inset, bottom) precipitates. The large one is of the type used in the statistical analysis.

precipitate, labeled by position vectors x_i, $i = 1, 2, \ldots, v$. Denoting the mean position by $\bar{x} = \frac{1}{v}\sum_{i=1}^{v} x_i$, we constructed a positive-definite symmetric tensor $\mathbf{B}$ using the formula:

$$\mathbf{B} = \frac{3}{v}\sum_{i=1}^{v}(x_i - \bar{x}) \otimes (x_i - \bar{x}) \tag{1}$$

The ellipsoid given by the equation $(x - \bar{x}) \cdot \mathbf{B}^{-1}(x - \bar{x}) = 1$ then gives an approximate representation of the precipitate. Equivalently, the set of points of the form $\mathbf{V}x + \bar{x}$ where $|x| = 1$ and $\mathbf{V} = \sqrt{\mathbf{B}}$ describes the same ellipsoid.[2] The unit eigenvector corresponding to the largest eigenvalue of $\mathbf{B}$ (or $\mathbf{V}$) is used below to define the direction of elongation. $\mathbf{B}$ was calculated for each of 27 of the larger precipitates and the corresponding directions of elongation are plotted in Figs. 2 and 3. The cones shown in these figures are explained below.

3. Determination of the transformation stretch tensor

The hypothesis of this paper is that suitably chosen sublattices of PbTe and Sb_2Te_3 are related by a deformation, and some aspects of the morphology of the precipitates are determined by a weak compatibility condition based on this deformation. To our knowledge, there is no systematic procedure for obtaining this deformation. There are an infinite number of possible choices, given that any such deformation can be preceded by a lattice-invariant deformation of one lattice and followed by a lattice-invariant deformation of the other. Beginning from the known structures [26], our procedure was to consider a large finite number of not-too-rare Te Bravais sublattices (as Te is contained in both phases) and to compare first their unit cell volumes, and then their detailed structures. The choices of sublattices were also

---
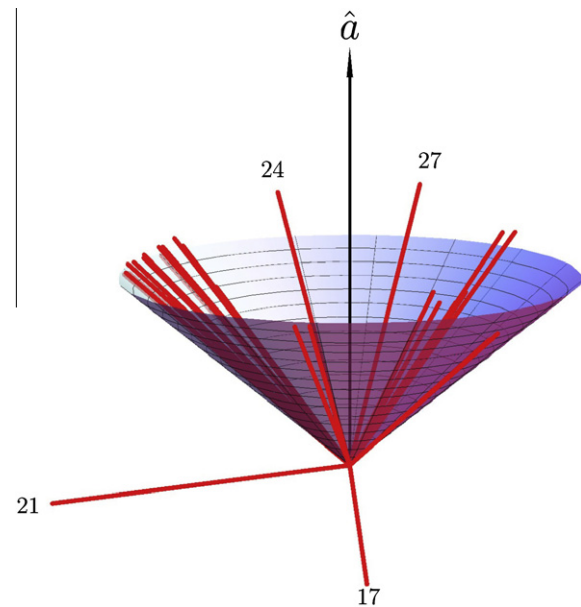[2] $\mathbf{V}$ is the unique positive-definite tensor satisfying $\mathbf{V}^2 = \mathbf{B}$.

Fig. 2. Plot of the directions of elongation of 27 precipitates together with a cone having a half-angle of 49.30°, as predicted by theory.

guided in part by Ikeda et al. [27,18], where orientation relationships are given as $(0\,0\,0\,1)_{Sb_2Te_3} \,|\, \{1\,1\,1\}_{PbTe}$ and $\langle 1\,1\,\bar{2}\,0 \rangle_{Sb_2Te_3} \,|\, \langle 1\,1\,0 \rangle_{PbTe}$ [18]. The resulting transformation stretch tensor $\mathbf{U}$ is illustrated in Fig. 4. It has the smallest value of $|\mathbf{U} - \mathbf{I}|$ among those examined.

The resulting deformation can be described as follows: every 6th stacking layer of $\{1\,1\,1\}_{PbTe}$ is translated along its normal to coincide with a $(0\,0\,0\,1)_{Sb_2Te_3}$ plane, and shrunk equally on two orthogonal directions in the $\{1\,1\,1\}_{PbTe}$ plane (Fig. 4). The sublattice correspondences between face-centered cubic (fcc) and hexagonal are:
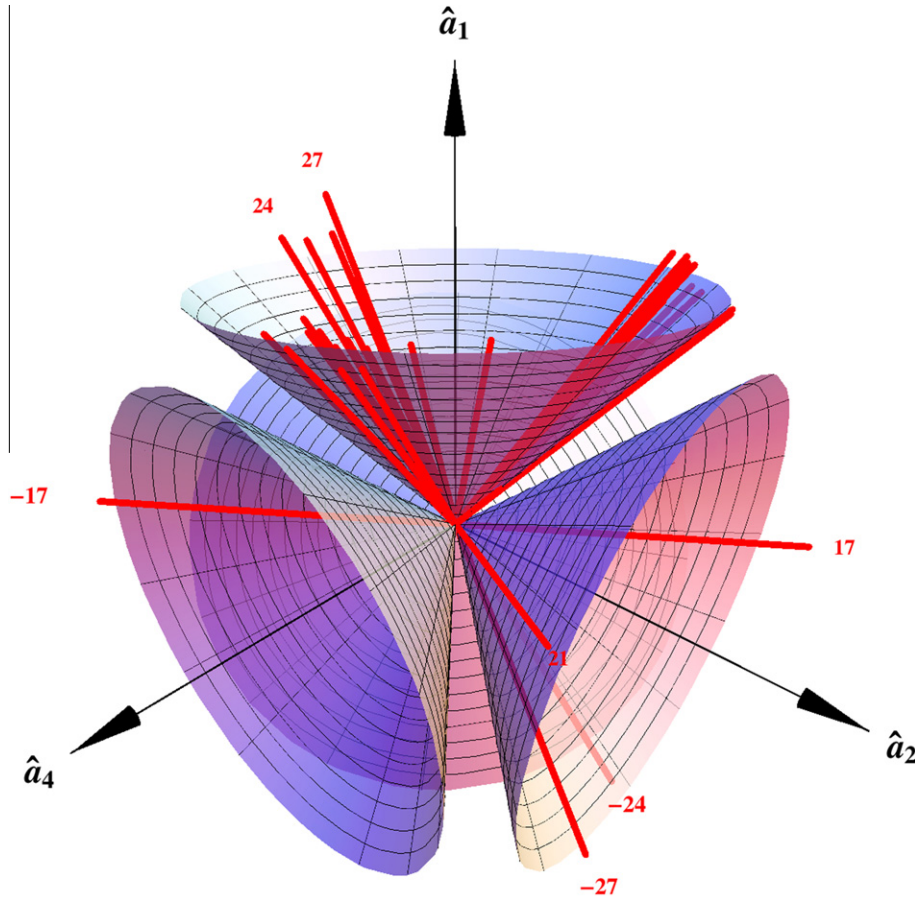
Fig. 3. The four crystallographically equivalent cones shown with 27 precipitates selected from the sample box, i.e. 17, 21, and the negatives of 27 and 24, match the $[\bar{1}11]$ cone variant, while the negative of 17 also matches the $[11\bar{1}]$ cone variant.

$$(2a_0, 2a_0, 2a_0)_{\text{fcc}} \rightarrow (0, 0, z_1 c)_{\text{hex}},$$

$$\left(-\frac{a_0}{2}, \frac{a_0}{2}, 0\right)_{\text{fcc}} \rightarrow \left(\frac{a}{2}, -\frac{\sqrt{3}a}{2}, 0\right)_{\text{hex}}, \qquad (2)$$

$$\left(0, -\frac{a_0}{2}, \frac{a_0}{2}\right)_{\text{fcc}} \rightarrow \left(\frac{a}{2}, \frac{\sqrt{3}a}{2}, 0\right)_{\text{hex}}.$$

Referred to an orthonormal basis parallel to the cubic axes of PbTe, the transformation stretch tensor is:

$$\mathbf{U} = \frac{1}{3}\begin{bmatrix} 2\lambda_1 + \lambda_3 & \lambda_3 - \lambda_1 & \lambda_3 - \lambda_1 \\ \lambda_3 - \lambda_1 & 2\lambda_1 + \lambda_3 & \lambda_3 - \lambda_1 \\ \lambda_3 - \lambda_1 & \lambda_3 - \lambda_1 & 2\lambda_1 + \lambda_3 \end{bmatrix}, \qquad (3)$$

where

$$\lambda_1 = \lambda_2 = \frac{\sqrt{2}a}{a_0} = 0.938269, \quad \lambda_3 = \frac{z_1 c}{2\sqrt{3}a_0} = 1.07786 \qquad (4)$$

and from Villars [26]: $a_0 = 6.429997$ Å, $a = 4.2665024$ Å, $c = 30.498837$ Å, $z_1 = 0.78719$ Å.

We note that $\mathbf{U}$ describes the stretch of the PbTe lattice. There is expected also to be a superimposed rigid rotation of the PbTe lattice. This rigid rotation is partly determined by the compatibility condition formulated below.

By symmetry, the elongation shown in Fig. 4 can occur along any of the family of $[111]_{\text{PbTe}}$ directions.

4. Formulation of a weak compatibility condition

Given two lattices related by a positive-definite symmetric stretch tensor $\mathbf{U}$ having ordered eigenvalues $\lambda_1 \leqslant \lambda_2 \leqslant \lambda_3$, a necessary and sufficient condition for the existence of an undistorted plane separating the lattices is that $\lambda_2 = 1$ [5]. Mathematically, if $\lambda_2 = 1$, then there is a rotation tensor $\mathbf{R}$ and vectors $\boldsymbol{a}$, $\boldsymbol{n}$ such that $\mathbf{R}\mathbf{U} - \mathbf{I} = \boldsymbol{a} \otimes \boldsymbol{n}$. The geometric interpretation is the following: $\mathbf{R}$ is the rotation needed to bring the distorted lattice into coincidence with the undistorted lattice on the plane, $\boldsymbol{n}$ is the normal to the plane, and $\boldsymbol{a}$ describes the shear of the lattice undergoing distortion and rotation. The sublattices of PbTe and Sb_2Te_3 related by the stretch tensor (3) do not have such an undistorted plane, because none of the eigenvalues of $\mathbf{U}$ given in (4) is near 1.

Instead of $\mathbf{R}\mathbf{U} - \mathbf{I}$ being a rank-one matrix $\boldsymbol{a} \otimes \boldsymbol{n}$ as above, we explore the condition that it is a rank-two matrix:

$$\mathbf{R}\mathbf{U} - \mathbf{I} = \boldsymbol{a}_1 \otimes \boldsymbol{n}_1 + \boldsymbol{a}_2 \otimes \boldsymbol{n}_2, \qquad (5)$$
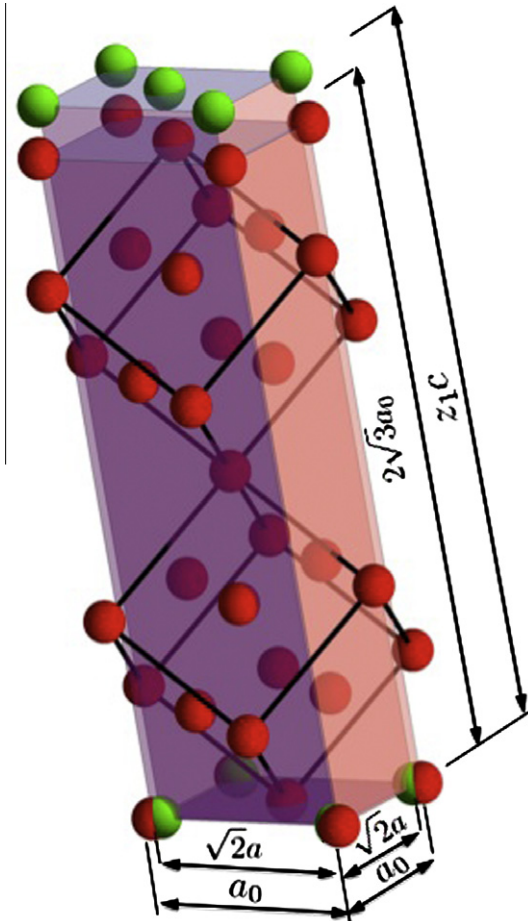
Fig. 4. The hypothesized transformation stretch maps the Te sublattice of PbTe (red) to a corresponding sublattice of Sb_2Te_3 (green) by elongation along $[111]_{PbTe}$. (For interpretation of the references to color in this figure legend, the reader is referred to the web version of this article.)

for some vectors a_1, n_1, a_2, n_2. This condition also has a convenient interpretation in terms of matching of the lattices. The condition (5) says that the distorted lattice, after a suitable rigid body rotation R, has a single direction e that is undistorted. That is, a direction in the original lattice is mapped to a parallel direction by the linear transformation RU and undergoes no lengthening or shortening. The vectors n_1, n_2 can be taken as orthonormal without loss of generality, and they have the geometric interpretation as vectors perpendicular to the undistorted direction e. The vectors a_1 and a_2 describe the shear in the planes spanned by n_1, e and n_2, e, respectively. A condition on U that is equivalent to (5) is that e, $|e| = 1$, satisfies:

$$RUe = e. \tag{6}$$

In turn, a necessary and sufficient condition on U that there is a rotation tensor R and unit vector e satisfying (6) is that the largest and smallest eigenvalues of U satisfy $\lambda_1 \leqslant 1 \leqslant \lambda_3$. The latter can be easily seen geometrically. The eigenvalues λ_1, λ_3 of U describe the least and greatest stretch experienced by lines in the reference lattice (in the case above, PbTe). If $\lambda_1 \leqslant 1 \leqslant \lambda_3$, then by continuity there

must be a line that undergoes no stretch, $|Ue| = |e| = 1$. R can then be used to rotate Ue into e. Conversely, if 1 is not between λ_1 and λ_3, then all lines are either shortened or lengthened, and there can be no vector $e \neq 0$ such that $|Ue| = |e|$.

We remark that the condition $RU - I = a \otimes n$ has a macroscopic interpretation. It is necessary and sufficient that there is a continuous deformation $y(x)$ having gradients $\nabla y = RU$ for $x \cdot n > c$ and $\nabla y = I$ for $x \cdot n < c$. Because of this fact, "rank-one connections" arise naturally in continuum theories of coherent phase transformations. Under the weaker compatibility condition $RU - I = a_1 \otimes n_1 + a_2 \otimes n_2$ with the nondegeneracy conditions $n_1 \nparallel n_2$, $a_1 \nparallel a_2$, there is no continuous function $y(x)$ satisfying $\nabla y = RU$ for $x \cdot n > c$ and $\nabla y = I$ for $x \cdot n < c$. Thus, under the weaker compatibility condition there is necessarily an elastic transition layer (not involving the deformation gradients RU and I) or possibly discontinuities. The latter indicate the presence of interface dislocations at the atomic level, which are seen in the present alloy [28].

If (6) holds for some e as discussed above, the rotation R is not unique. Geometrically, the axis of R must be on a plane that bisects e and Ue but it can be any vector on that plane. In the generic case $Ue \nparallel e$ there is clearly one parameter of freedom of R. A convenient way to quantify this nonuniqueness is to observe that if a rotation R satisfies $RUe = e$, then so does $R_\theta R$, where $R_\theta e = e$ and R_θ has angle of rotation θ. Later, we will have to determine θ by energy minimization.

There is also nonuniqueness of the undistorted direction. Supposing that the ordered eigenvalues of U satisfy $\lambda_1 \leqslant 1 \leqslant \lambda_3$ so there is at least one undistorted direction, then the set of solutions $|e| = 1$ of $|Ue| = 1$ lies on a (possibly distorted) cone. This is easiest to see geometrically. The set of points of the form Uv, $|v| = 1$, is an ellipsoid, the strain ellipsoid of U. The condition $|Ue| = |e| = 1$ says that there is a point on this ellipsoid with length 1. The set of all such points is the intersection of the ellipsoid with the unit sphere, which is clearly a distorted cone. (This can be proved analytically, and the equation of the cone is easily determined.) In the degenerate cases $\lambda_3 = 1 > \lambda_2$ or $1 = \lambda_1 < \lambda_2$ the intersection of the cone with the sphere degenerates to two points.

In our case (3), (4) the cone has circular cross-section, because $\lambda_1 = \lambda_2 < 1 < \lambda_3$. In fact, in our case U can be written:

$$U = \lambda_1 I + (\lambda_3 - \lambda_1)e_3 \otimes e_3, \quad e_3 = \frac{1}{\sqrt{3}}[111]. \tag{7}$$

By direct calculation, $|Ue|^2 = |e|^2 = 1$ becomes:

$$e \cdot e_3 = \pm \sqrt{\frac{1 - \lambda_1^2}{\lambda_3^2 - \lambda_1^2}} \tag{8}$$

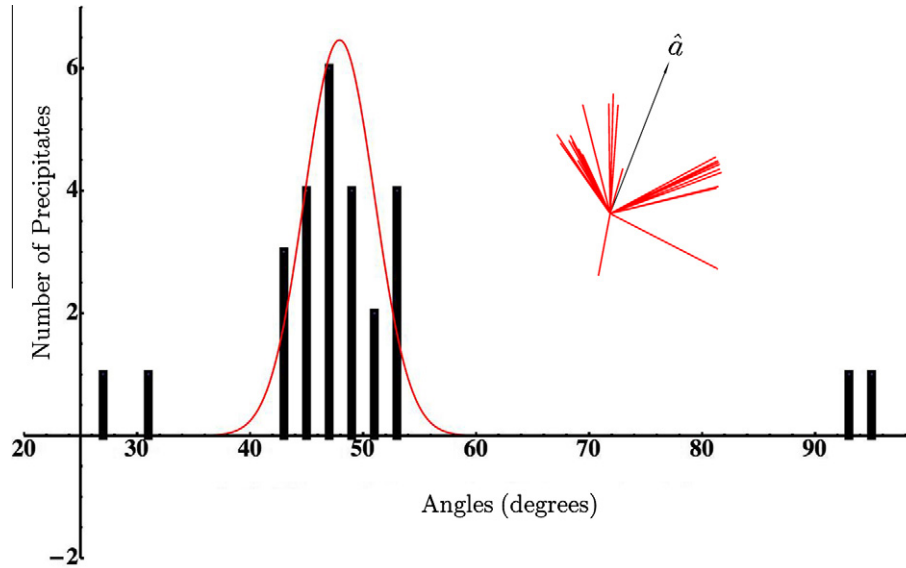which describes a cone with a circular cross-section. The half-angle of this cone is:

Fig. 5. Histogram of angles between the directions of elongation of the precipitates and cone axis $\hat{a}$. The Gaussian fit to this data has average half-angle 47.20° and standard deviation 2.94°.

$$\psi = \arccos \sqrt{\frac{1-\lambda_1^2}{\lambda_3^2 - \lambda_1^2}}. \tag{9}$$

The crystallographically equivalent cones are obtained by replacing $[1\,1\,1]$ in (7) by, respectively, $[\bar{1}\,1\,1]$, $[1\,\bar{1}\,1]$ and $[1\,1\,\bar{1}]$.

Using the eigenvalues (4) measured from the crystal structures, we calculate from (9) that the predicted half-angle of the undistorted cone is $\psi = 49.30°$.

5. Structure of the precipitates and comparison with the weak compatibility condition

We selected 27 of the larger precipitates from the reconstruction shown in Fig. 1, determined their directions of elongation by the method described after Eq. (1), and plotted these principal axes in Fig. 2. On the same figure we plot a cone with the half-angle $\psi = 49.30°$ determined from the weak compatibility condition. The axis of this cone was allowed to vary so as to give a best fit to these directions. This axis is in principle known from the stretch tensor. An experimental determination of $\hat{a}$ was not possible as the imaging procedures could not measure the absolute orientation with sufficient accuracy.

The measured directions give reasonable agreement with the cone, except for two of the precipitates labeled 17 and 21. A histogram of the angular deviations of the measured directions of elongation and the cone axis is shown in Fig. 5. This was fitted with a Gaussian distribution as shown in Fig. 5, after omitting the precipitates 17 and 21. The standard deviation based on this Gaussian is 2.94°.

The directions of elongation of precipitates 17 and 21, and incidentally also the negatives of 24 and 27, agree well with two of the other crystallographic variants as shown in Fig. 3. Evidently, the abundance of directions corresponding to just one crystallographic variant is related to a collective effect known from elastic homogenization theory, in which energy minimization of periodic distributions of precipitates often leads to alignment.

6. Analysis of the shapes of precipitates

We now explore the detailed shapes of the precipitates using linearized elasticity theory. This has the advantage of allowing the methods of Eshelby [29] to be used, but the disadvantage of losing some accuracy due to its inherent geometric approximations. However, geometric linearization does preserve the rank-two compatibility condition in the following sense: $|\mathbf{U}e| = |e|$ linearizes[3] to $e \cdot \mathbf{E}e = 0$, where $\mathbf{E}$ is the infinitesimal strain tensor.

The use of linearized elasticity is justified under the approximation that the deformation gradient is near $\mathbf{I}$, which in the present situation implies that $|\mathbf{RU} - \mathbf{I}|$ is small. This has implications for the rotation $\mathbf{R}$, which as discussed in Section 4 is not unique. To examine this freedom, note that a natural choice of $\mathbf{R}$ has axis parallel to $\mathbf{U}e \times e$. Let $\mathbf{R}$ be the rotation with axis parallel to $\mathbf{U}e \times e$ that satisfies $\mathbf{RU}e = e$. Now, as discussed in Section 4, the rotation is not unique, and $\mathbf{R}_\theta \mathbf{RU}e = e$ also holds, as long as $\mathbf{R}_\theta$ has axis e. We claim that the choice of θ that best justifies the linearized theory, i.e. that minimizes $|\mathbf{R}_\theta \mathbf{RU} - \mathbf{I}|$, is the choice $\theta = 0$, i.e. $\mathbf{R}_\theta = \mathbf{I}$. That follows because by direct calculation:

$$|\mathbf{R}_\theta \mathbf{RU} - \mathbf{I}| = \sqrt{1 + 2\lambda_1^2 + \lambda_3^2 - 2\lambda_1(1 + \lambda_3)\cos\theta}, \tag{10}$$

---

[3] Write $\mathbf{U} = \mathbf{I} + \mathbf{E}$, substitute into the condition $e \cdot \mathbf{U}^2 e = |e|^2$, and neglect terms of order $|\mathbf{E}|^2$.
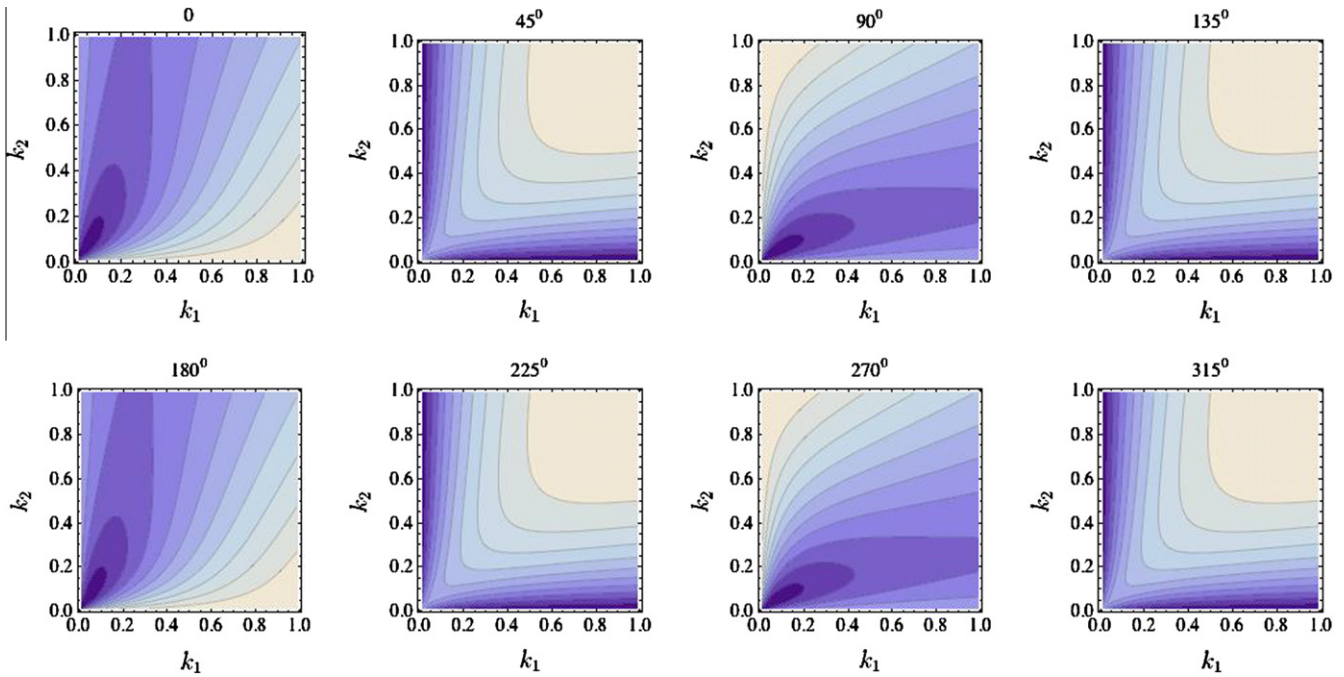
Fig. 6. Contour plot of linearized energy density with respect to its eccentricities at different orientations of the ellipsoid. All ellipsoids have long axis parallel to the **e** axis. See text.

which is minimized at $\theta = 0$. The condition $\theta = 0$ also has the pleasing interpretation from nonlinear theory that the maximum displacement of points in the reference cubic lattice to their positions in the deformed lattice is minimized.

For the purpose of linearized theory we make the obvious choice of eigenstrain:

$$\mathbf{E}^{\star} = \mathbf{U} - \mathbf{I}. \tag{11}$$

Eshelby's method [29] delivers an exact solution of the equations of linearized elasticity for an ellipsoidal inclusion Ω in an infinite medium, satisfying continuity of displacement and traction at the boundary of the inclusion. On the inclusion, the stress–strain law is $\sigma = \mathbb{C}(\mathbf{E} - \mathbf{E}^{\star})$, while outside the inclusion it is $\sigma = \mathbb{C}\mathbf{E}$, where $\mathbb{C}$ is the (fourth-order) elasticity tensor of the material. Eshelby's way [29] of explaining the solution in a physical sense is to imagine cutting out the ellipsoid Ω from the reference configuration, to allow it to strain to a stress-free state with the eigenstrain $\mathbf{E}^{\star}$, to force it back into the matrix satisfying displacement continuity, and to allow both the inclusion and surrounding matrix to relax. A necessary condition is that the final stress and strain on the inclusion are constants. Since the problem is linear and the strain on the inclusion vanishes when the eigenstrain vanishes, the strain on the inclusion can be expressed

$$\mathbf{E}^{I} = \frac{1}{2}(\nabla \boldsymbol{u} + \nabla \boldsymbol{u}^{T}) = \mathbb{S}\mathbf{E}^{\star} \quad \text{on } \Omega. \tag{12}$$

The fourth-order tensor $\mathbb{S}$ is known as the Eshelby tensor. It only depends on the elastic constants and Ω, and it takes a relatively simple form in the orthonormal basis of

eigenvectors of Ω for isotropic materials [30]. The stress on the inclusion is $\sigma^{I} = \mathbb{C}(\mathbb{S}\mathbf{E}^{\star} - \mathbf{E}^{\star})$. The total energy of the inclusion and its exterior also assumes the simple algebraic form:

$$-\frac{vol(\Omega)}{2}\sigma^{I} \cdot \mathbf{E}^{\star} = \frac{vol(\Omega)}{2}\mathbf{E}^{\star} \cdot \mathbb{C}(\mathbf{E}^{\star} - \mathbb{S}\mathbf{E}^{\star}). \tag{13}$$

In the absence of measurements of the full set of elastic moduli of either phase we chose the simple isotropic form. For the calculations below we used the moduli estimated from Ref. [31]: Young's modulus $E = 57$ GPa, and Poisson's ratio $v = 0.26$. We performed each energy calculation given below on the basis of the principal axes of the ellipsoid, in which the Eshelby tensor only depends on the elastic moduli and two eccentricities $k_1 = a_1/a_3$ and $k_2 = a_2/a_3$, where a_1, a_2, a_3 are the lengths of the principal axes, with a_3 the long principal axis, which was always taken to be in the direction $\boldsymbol{e}$.

We first examined the effect of orientation of the ellipsoid. We rotated the principal axes of the ellipsoid around its (fixed) long axis by angles $0°$, $45°$, $90°$, $135°$, $180°$, $225°$, $270°$ and $315°$ measured from $\mathbf{U}\boldsymbol{e} \times \boldsymbol{e}$. For each such angle we plotted the total energy (divided by $vol(\Omega)$) as a function of the two eccentricities k_1 and k_2. The results are shown in Fig. 6. The eccentricities were taken to be in the domains $0 < k_1 \leqslant 1$ and $0 < k_2 \leqslant 1$. Experiments with larger values of k_1, k_2 always resulted in higher energies, consistent with the hypothesis that the long axis was $\boldsymbol{e}$, as assumed. The graphs at $90°$ and $270°$ are symmetry-related to the graphs at $0°$ and $180°$, respectively, the symmetry transformation being the exchange of the principal axes 1 and 2 of the
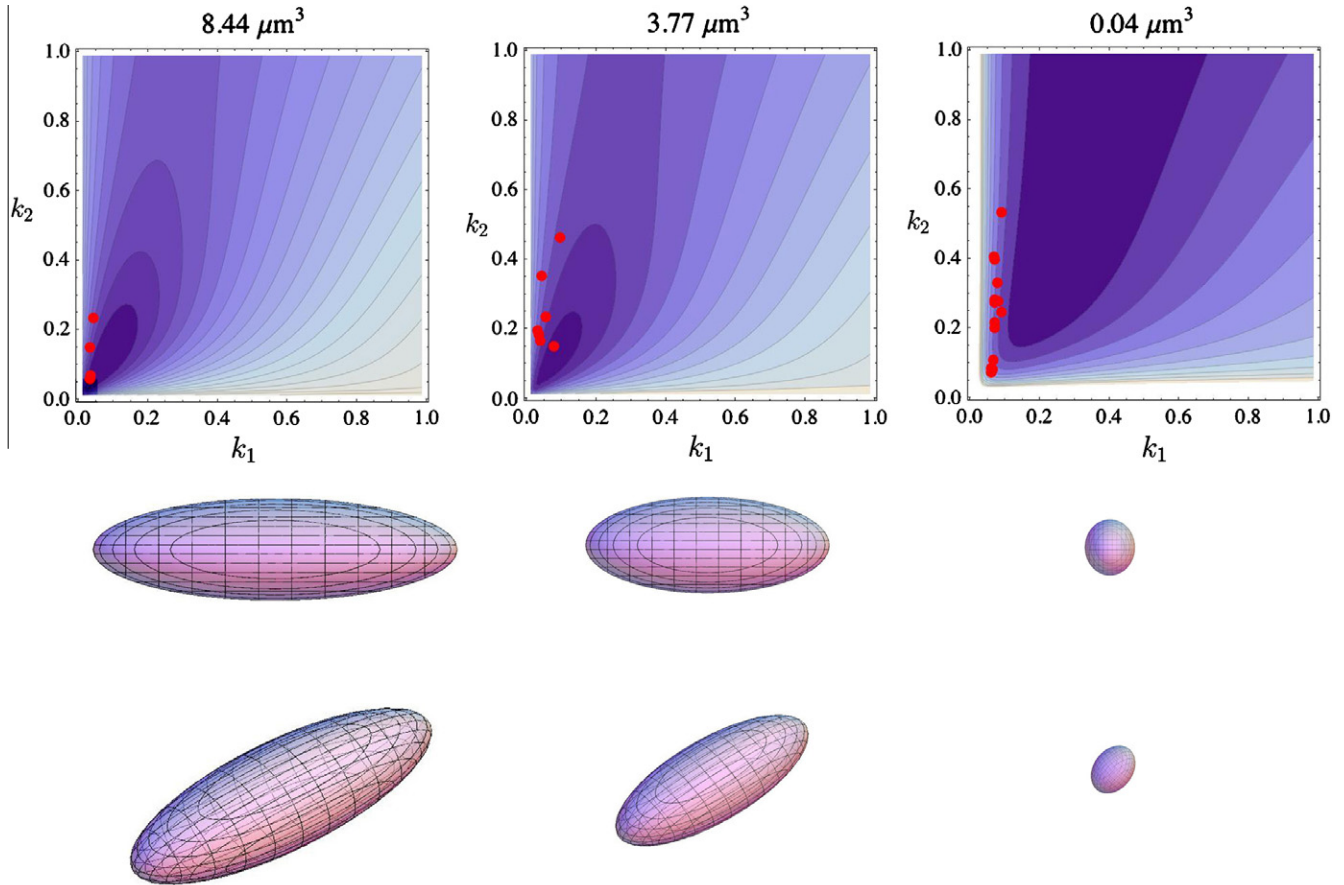
Fig. 7. Total elastic plus interfacial free energy contours as a function of the eccentricities k_1 and k_2 at three volumes: 8.44, 3.77 and 0.04 μm^3 (left to right). Two views of the shapes of the energy-minimizing ellipsoidal inclusions in each case are below the graphs. The red dots are experimentally measured values of k_1 and k_2 for precipitates having volumes in the range $(V-1, V+1)$ where $V = 8.44$, 3.77, 0.04 μm^3, respectively. (For interpretation of the references to colour in this figure legend, the reader is referred to the web version of this article.)

ellipsoid. The lowest energy among all the plots is found very close[4] to $k_1 = k_2 = 0$ in the 0° and 180° plots (and by symmetry in 90° and 270°). This suggests the predominance of the elongated shapes. However, there is considerable asymmetry in these plots for small but nonzero values of k_1 and k_2, suggesting also more of a ribbon-like shape.

These results suggest that interfacial energy is also playing a role, both preventing the growth of extremely elongated ribbons and possibly also significantly affecting the shapes of small precipitates. Hence we consider both elastic energy and interfacial energy. Denoting the elastic energy (divided by $vol(\Omega)$) determined above at angle 0° by $\phi(k_1, k_2)$, we now consider a total energy:

$$\mathscr{E}(k_1, k_2) = \phi(k_1, k_2) + \gamma A(k_1, k_2) \qquad (14)$$

where $A(k_1, k_2)$ denotes the surface area of the ellipsoid divided by $vol(\Omega)$, and γ is the interfacial energy per unit area.

Fig. 7 shows the total free energy density $\mathscr{E}$ of different precipitates and their corresponding shapes at three different volumes: 8.44, 3.77 and 0.04 μm^3. To do this

calculation a particular value of γ was needed and this was adjusted to give reasonable agreement with the shapes seen in the reconstruction above at the corresponding volumes. The interfacial energy constant that gives the plots in Fig. 7 is $\gamma = 250$ dyn cm^{-1}. There is signficant scatter in the experimental values of k_1 and k_2 and the reconstructed shapes are somewhat more flattened. However, we also note that the calculated energy vs. eccentricity is very flat near the minimum in all three graphs. The scatter could easily be caused by the likely strong interactions between precipitates, which is missed by the Eshelby calculation. Other reasons for this deviation could be elastic or interfacial anisotropy (which was not included), the differing elastic tensors of the two phases, a possible lack of coherence that is necessarily assumed by the Eshelby method, or errors due to geometric linearization.

7. Conclusions and recommendations

In summary, we propose a simple, weak compatibility condition for precipitation in Sb$_2$Te$_3$/PbTe thermoelectric composites, which is expected to be applicable to the growth of Widmanstä tten microstructure precipitates in

---

[4] The fact that it does not occur precisely at $k_1 = k_2 = 0$ is very likely due to discretization error associated with ribbon-like ellipsoids.

general. This criterion is consistent with a partial lack of coherence. The condition is expressed as a "rank-two" connection between the identity and a deformation gradient tensor describing the transformation of a suitable sublattice. In the case we studied, the weak compatibility condition implies the presence of four crystallographically equivalent cones, on which the long directions of the ribbon-like precipitates are predicted to lie. The shapes are also compared to an Eshelby calculation that uses geometrically linear theory and full coherence. This comparison suggests an interfacial energy of 250 dyn cm^{-1} and a transition from sphere to flattened disk to ribbon to needle as the precipitate grows larger.

Any influence that changes the deformation gradient tensor will change the cone. Either flat or narrow cones imply alignment of percipitates. The natural choice of influence is stress. An estimate of how stress changes the lattice parameters of the two phases is needed for a quantitative analysis.

References

[1] Wechsler MS, Lieberman DS, Read RA. Trans AIME J Met 1953;197:1503.
[2] Ball JM, James RD. Arch Rat Mech Anal 1987;100:13.
[3] Shield TW. J Mech Phys Solids 1995;43:869.
[4] Hane KF, Shield TW. J Elasticity 2000;59:267.
[5] Zhang Z, James RD, Mü ller S. Acta Mater 2009;57:4332.
[6] Cui J, Chu Y, Famodu O, Furuya Y, Hattrick-Simpers J, James RD, et al. Nat Mater 2006;5:286.
[7] Zarnetta R, Takahashi R, Young ML, Savan A, Furuya Y, Thienhaus S, et al. Adv Funct Mater 2010;20:1917.
[8] Sutou Y, Omori T, Kainuma R, Ishida K. Mater Sci Technol 2008;24:896.
[9] Srivastava V, Chen X, James RD. Appl Phys Lett 2010;97:014101.
[10] Srivastava V, Song Y, Bhatti K, James RD. Adv Energy Mater 2011;1:97.
[11] Delville R, Kasinathan S, Zhang Z, Humbeeck V, James R, Schryvers D. Phil Mag 2010;90:177.
[12] Aksoy S, Posth O, Acet M, Meckenstock R, Lindner J, Farle M, et al. J Phys: Conf Ser 2010;200:092001.
[13] Hu F, Wang J, Shen J, Gao B, Sun J, Shen B. J Appl Phys 2009;105:07A940.
[14] Fujino S, Murakami M, Anbusathaiah V, Lim S, Nagarajan V, Fennie CJ, et al. Appl Phys Lett 2008;92:202904.
[15] Xie S, Li Y, Qiao Y, Liu Y, Lan L, Zhou Y, et al. Appl Phys Lett 2008;92:062901.
[16] Meethong N, Huang HS, Speakman SA, Carter WC, Chiang Y. Adv Funct Mater 2007;17:1115.
[17] Louie MW, Kislitsyn M, Bhattacharya K, Haile SM. Solid State Ion 2010;181:173.
[18] Ikeda T, Ravi VA, Snyder GJ. Acta Mater 2009;57:666.
[19] Medlin DL, Snyder GJ. Current Opin Colloid Interface Sci 2009;14:226.
[20] Kanatzidis MG. Chem Mater 2010;22:648.
[21] Pei Y, Lensch-Falk J, Toberer ES, Medlin DL, Snyder GJ. Adv Funct Mater 2010. doi:10.1002/adfm.201000878.
[22] Jeng M-S, Yang R, Song D, Chen G. J Heat Transfer 2008;130:042410.
[23] Cao S, Tirry W, Van den Broek W, Schryvers D. J Microsc 2009;233:6168.
[24] Cao S, Somsen C, Croitoru M, Schruyvers D, Eggeler G. Scripta Mater 2010;62:399.
[25] Ikeda T, Marolf NJ, Bergumb K, Toussaint MB, Heinz NA, Ravic VA, et al. Acta Mater 2011;59:2679.
[26] Villars P. Pearson's handbook: crystallographic data for intermetallic phases. Materials Park (OH): ASM International; 1991. vol. 4: 4897, 5195.
[27] Ikeda T, Collins LA, Ravi VA, Gascoin FS, Haile SM, Snyder J. Chem Mater 2007;19:763.
[28] Heinz N, Medlin D, Snyder J. accompanied by HREM micrograph of an interface dislocation at the PbTe–Sb$_2$Te$_3$ interface, personal communication.
[29] Eshelby JD. Proc Roy Soc 1957;A241:376.
[30] Toshio M. Micromechanics of defects in solids. Dordrecht: Martinus Nijhoff; 1987. p. 77.
[31] Ren F, Case ED, Sootsman JR, Kanatzidis MG, Kong H, Uher C, et al. Acta Mater 2008;56:5954.